Facile Synthesis of Fe@C Loaded on g-C$_3$N$_4$ for CO$_2$ Electrochemical Reduction to CO with Low Overpotential

Lina Zhang, Ying Zhang, Baikang Zhu, Jian Guo, Dongguang Wang, Zhongqi Cao, Lihui Chen, Luhui Wang, Chunyang Zhai,* and Hengcong Tao*

ACCESS | Metrics & More | Article Recommendations

ABSTRACT: Electrochemical CO$_2$ reduction has been acknowledged as a hopeful tactic to alleviate environmental and global energy crises. Herein, we designed an Fe@C/g-C$_3$N$_4$ heterogeneous nanocomposite material by a simple one-pot method, which we applied to the electrocatalytic CO$_2$ reduction reaction (ECR). Our optimized 20 mg-Fe@C/g-C$_3$N$_4$-1100 catalyst displays excellent performance for the ECR and a maximum Faradaic efficiency (FE) of 88% with a low overpotential of −0.38 V *vs.* RHE. The Tafel slope reveals that the first electron transfer, which involves a surface-adsorbed *COOH intermediate, is the rate-determining step for 20 mg-Fe@C/C$_3$N$_4$-1100 during the ECR. More precisely, the coordinating capability of the g-C$_3$N$_4$ framework and Fe@C species as a highly active site promote the intermediate product transmission. These results indicate that the combination of temperature adjustment and precursor optimization is key to facilitating the ECR of an iron-based catalyst.
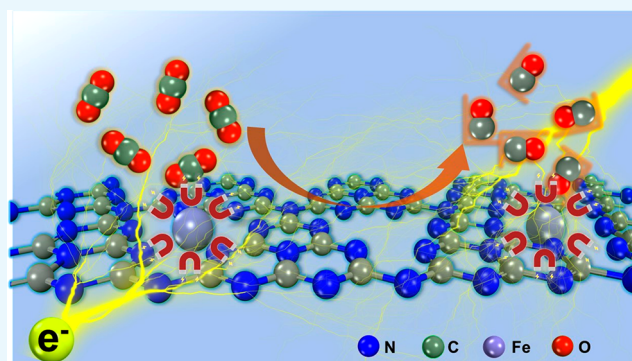
INTRODUCTION

The rising carbon dioxide (CO$_2$) concentration in the atmosphere, which causes a variety of problems such as global warming, aggravation of desertification, and a decline in biodiversity, is gradually threatening the sustainable development of human beings.[1−4] Electrochemical reduction of CO$_2$, which can be powered by electricity from renewable sources, is considered to be a potential efficient way to transform CO$_2$ into value-added fuels and chemical feedstocks.[5−7] However, the electrochemical CO$_2$ reduction reaction (ECR) is impeded by the high overpotential and poor selectivity due to the high energy barriers of CO$_2$ and the hydrogen evolution reaction (HER).[8,9] For these reasons, the exploration of efficient, original, and useful electrode materials for the ECR is significant at this current stage.

Recently, carbon-based catalysts, as abundant and cheap materials, have been considered to be hopeful electrocatalytic carbon dioxide candidates due to their high specific surface area, remarkable electrical conductivity, and outstanding chemical stability.[10−12] However, pure carbon catalysts display no activity for CO$_2$ valorization which therefore hampers their roles in the electrocatalytic CO$_2$ process. On the grounds of experimental research, we know that a transition metal (e.g., Fe,[13] Co,[14] Ni,[15] and Mn[16]) anchored on a carbon-based material can enable an apparent catalytic activity to improve the efficiency and selectivity of ECR. Especially, Li et al.[17]

verified that, a superb proton activation capability, the Fe dopant could reduce the reaction barriers and decrease the overpotential. Hence, it is feasible to develop an Fe@C material to assist in electrochemical catalysis reactions.

Furthermore, loading an Fe@C material onto support materials is a useful strategy to avoid reunion. An ideal support material not only offers a large surface area during the electrocatalytic reactions but also accelerates abundant interface links between the carrier and the metal nanoparticles. For example, Zhang et al.[18] investigated detailed mechanisms of Fe/g-C$_3$N$_4$, Co/g-C$_3$N$_4$, and Ni/g-C$_3$N$_4$ catalysts for electrochemical CO$_2$ reduction. Fe/g-C$_3$N$_4$ showed the highest electrocatalytic activity in comparison to Co/g-C$_3$N$_4$ and Ni/g-C$_3$N$_4$ in terms of the activity and stability. On the basis of the above research, g-C$_3$N$_4$, as a promising support material, has a strong affinity to CO$_2$ and high oxophilicity for adsorption of an adsorption intermediate.[19] Consequently, integrating g-C$_3$N$_4$ with Fe@C generates a stable product that constitutes part of a potential class of active catalysts for the ECR.
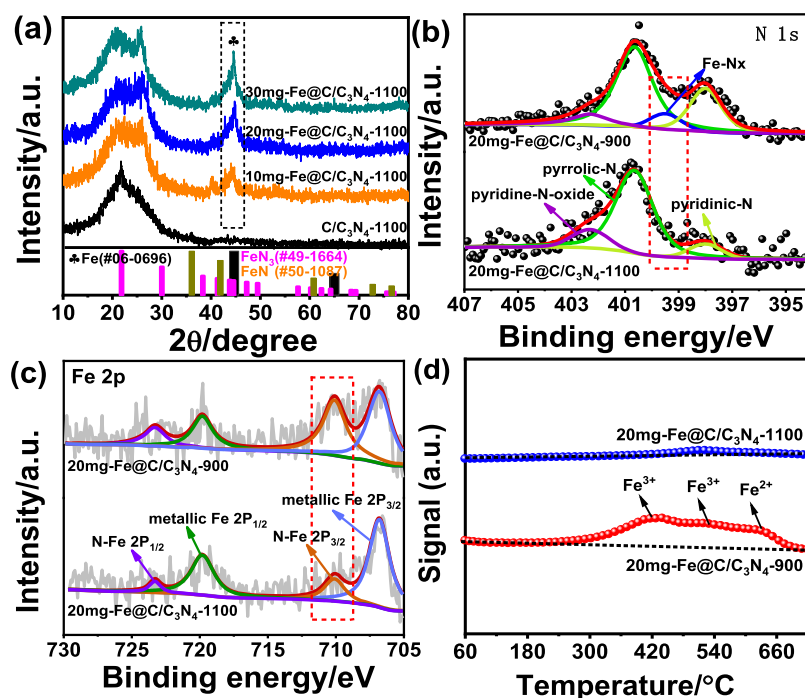
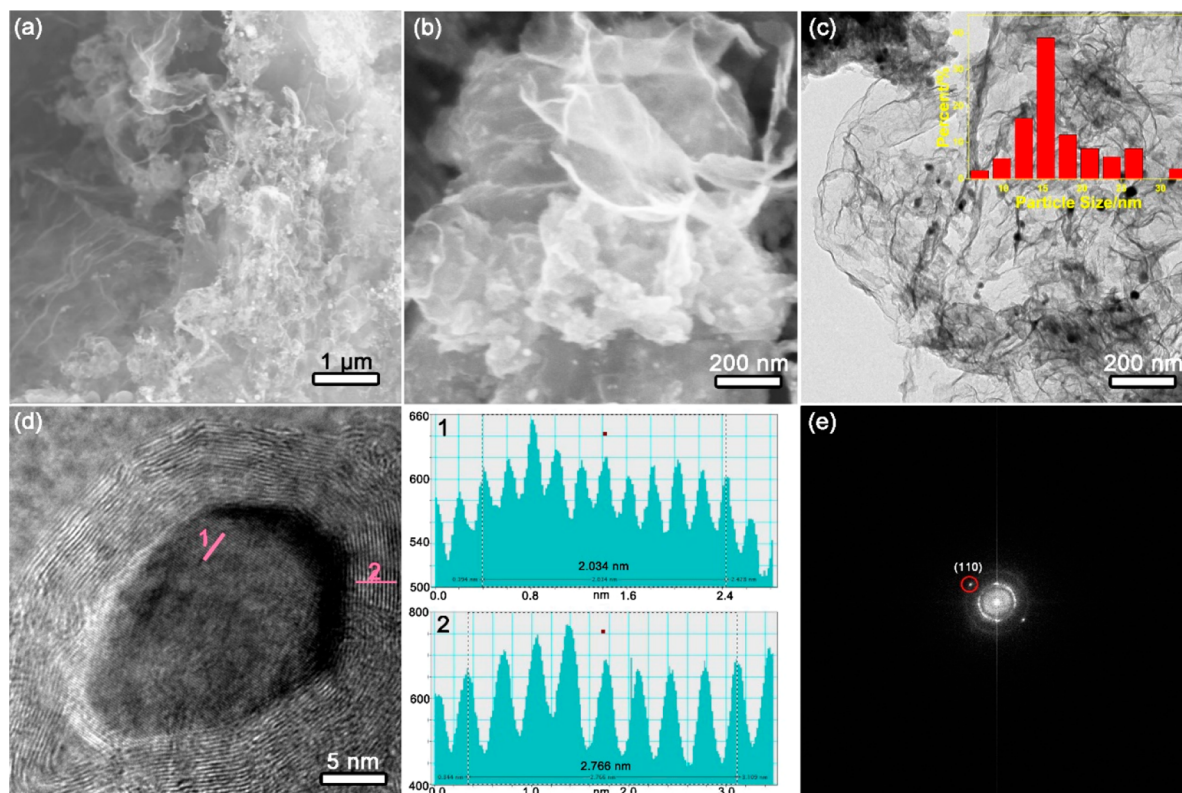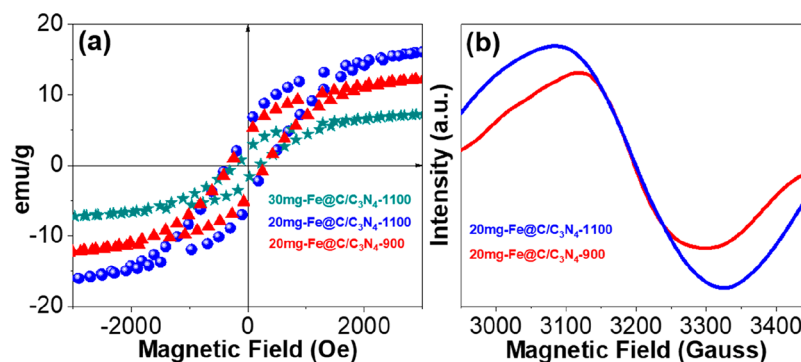**Figure 1.** (a) XRD patterns of C/C_3N_4-1100, 10 mg-Fe@C/C_3N_4-1100, 20 mg-Fe@C/C_3N_4-1100, and 30 mg-Fe@C/C_3N_4-1100. (b) N 1s and (c) Fe 2p XPS spectra of 20 mg-Fe@C/C_3N_4-1100 and 20 mg-Fe@C/C_3N_4-900. (d) H-TPR spectra of 20 mg-Fe@C/C_3N_4-1100 and 20 mg-Fe@C/C_3N_4-900.

Figure 2. (a, b) SEM images of 20 mg-Fe@C/C_3N_4-1100. (c, d) TEM images of 20 mg-Fe@C/C_3N_4-1100. Inset in (c): size distribution of Fe nanoparticles. (e) Fast Fourier transform (FFT) of the region shown in (d).

Herein, we report a Fe@C/g-C_3N_4 nanocomposite, where the Fe nanoparticles were uniformly deposited on the surface of g-C_3N_4 nanosheets. In addition, the composite catalyst was used in a traditional H-type cell assembly to complete the

experiment. In order to evaluate the high activity, long stability, and selectivity of the catalysts, a series of Fe@C/g-C_3N_4 catalysts with different amounts of Fe-based materials (0, 10, 20, and 30 mg) as well as different sintering temperatures (900

Figure 3. (a) VSM curves illustrating the saturation magnetization of 30 mg-Fe@C/C$_3$N$_4$-1100, 20 mg-Fe@C/C$_3$N$_4$-1100 and 20 mg-Fe@C/C$_3$N$_4$-900. (b) EPR spectra of 20 mg-Fe@C/C$_3$N$_4$-1100 and 20 mg-Fe@C/C$_3$N$_4$-900.

and 1100 °C) were synthesized for the process of the ECR. Additionally, the characterizations revealed the magnetism of 20 mg-Fe@C/C$_3$N$_4$-1100 created a new platform to boost the performance of the catalyst in electrocatalytic CO$_2$ reduction. Electrocatalytic performance tests confirmed that 20 mg-Fe@C/C$_3$N$_4$-1100 possessed the fastest charge transfer rate and the best selectivity. Potentially, the electrocatalyst material 20 mg-Fe@C/C$_3$N$_4$-1100 as a promising tool will open up a new pathway for the ECR.

RESULTS AND DISCUSSION

As shown in Figure 1a, all of the X-ray diffraction (XRD) patterns of 10 mg-Fe@C/C$_3$N$_4$-1100, 20 mg-Fe@C/C$_3$N$_4$-1100, and 30 mg-Fe@C/C$_3$N$_4$-1100 displayed one pronounced diffraction peak at approximately 44.7°, which corresponds to the (110) plane of Fe^0 (PDF #06-0696). A broad peak at close to 22° is derived from the (002) reflection of the graphitic carbon structure. Moreover, no other reflection peaks of iron nitride (PDF #49-1664 and #50-1087) were identified, suggesting the predominant formation of metallic Fe in the samples. By utilizing Scherrer's equation relating the coherently scattering domains with the Bragg peak widths, $L = \kappa\lambda/B \cos\theta$, in which $\kappa = 0.89$ for spherical particle and B is the full angular width at half-maximum of the peak in radians, the average crystal size was determined to be around 17.8 nm for 20 mg-Fe@C/C$_3$N$_4$-1100.[20] Moreover, we noted that improving the loading content of the iron precursor led to an increase in the particle size. Additionally, the particle size increased upon an increase in annealing temperature.

Subsequently, X-ray photoelectron spectroscopy (XPS) was employed to provide insight into the surface composition of the resulting 20 mg-Fe@C/C$_3$N$_4$-1100 and 20 mg-Fe@C/C$_3$N$_4$-900. A dominant N 1s peak at 400.7 eV was observed for both samples, which can be assigned to pyrrolic N.[21] An apparent peak at around 399.68 eV in 20 mg-Fe@C/C$_3$N$_4$-900, which disappeared in 20 mg-Fe@C/C$_3$N$_4$-1100, confirmed the presence of N similar to that of the Fe-N$_x$ moiety.[22,23] The content of the pyridinic N improved the predominant formation of iron.[24] The N−Fe 2p$_{3/2}$ binding energies (BEs) of 20 mg-Fe@C/C$_3$N$_4$-1100 were shifted to lower values in comparison with the BEs of 20 mg-Fe@C/C$_3$N$_4$-900 (Figure 1c), suggesting that 20 mg-Fe@C/C$_3$N$_4$-1100 composite material had more iron in comparison to the other samples.

To further characterize the redox properties of the prepared materials, H$_2$-TPR was used to describe 20 mg-Fe@C/C$_3$N$_4$-1100 and 20 mg-Fe@C/C$_3$N$_4$-900, as shown in Figure 1d.

Their H$_2$ consumption peaks, centered at approximately 410 and 520 °C, corresponding to the reduction of iron trioxide to ferrous ion,[25,26] were detected for 20 mg-Fe@C/C$_3$N$_4$-900. The last H$_2$ consumption peak (630 °C), corresponding to the reduction of Fe^{2+} to Fe^0, was relatively weak.[27] However, there was no obvious H$_2$ consumption peak for 20 mg-Fe@C/C$_3$N$_4$-1100, implying that the main component of this material was iron. Obviously, it has been confirmed that the H$_2$-TPR results were consistent with the XRD and XPS results.

The morphological properties of 20 mg-Fe@C/C$_3$N$_4$-1100 were characterized by scanning electron microscopy (SEM) and transmission electron microscopy (TEM). Figure 2a,b showed that the Fe nanoparticles were successfully deposited on the surface of g-C$_3$N$_4$ while the nanosheet structure remained intact. In addition, the size distribution histogram of Fe nanoparticles in 20 mg-Fe@C/C$_3$N$_4$-1100 was analyzed.[28] As can be seen from the inset of Figure 2c, the representative diameters are from 5 to 50 nm, and the average diameter is 15 nm. Moreover, the d spacing of 0.2014 nm in Figure 2d, which agreed well with the lattice space of the Fe (110) plane, confirmed the generation of Fe nanoparticles.[29,30] As shown in Figure 2e, the (110) plane of Fe was also confirmed by fast Fourier transform (FFT) of the region, as shown in Figure 2e. Therefore, TEM and HR-TEM further testified to the formation of the 20 mg-Fe@C/C$_3$N$_4$-1100 composite in this work.

The magnetic characteristics of Fe@C/C$_3$N$_4$ with different iron contents have been confirmed by VSM, and the magnetization curves are shown in Figure 3a. It was noted that 30 mg-Fe@C/C$_3$N$_4$-1100, 20 mg-Fe@C/C$_3$N$_4$-1100, and 20 mg-Fe@C/C$_3$N$_4$-900 had magnetic saturations of ∼7.5, 16, and 12.5 emu/g at an ∼3000 kOe field strength, respectively. As expected, 20 mg-Fe@C/C$_3$N$_4$-1100 had higher magnetic properties in comparison to the other samples.[31,32] More importantly, the prepared catalyst had certain magnetism, which provided a novel train of thought for the development of further different catalysts.[33] Additionally, the electron paramagnetic resonance (EPR) signal intensity of 20 mg-Fe@C/C$_3$N$_4$-1100 also increased in comparison to that of 20 mg-Fe@C/C$_3$N$_4$-900, implying that the Fe magnetic states had increased (Figure 3b).[34] To sum up, the 20 mg-Fe@C/C$_3$N$_4$-1100 precatalyst displayed a transformation of Fe microstructure and exhibited excellent magnetism.[29]

To evaluate the CO$_2$ reduction reaction activity of 20 mg-Fe@C/C$_3$N$_4$-1100, linear sweep voltammetry (LSV) measurements of a well-prepared catalyst/carbon paper was conducted with N$_2$-or CO$_2$-saturated 0.1 M KHCO$_3$ electrolytes from
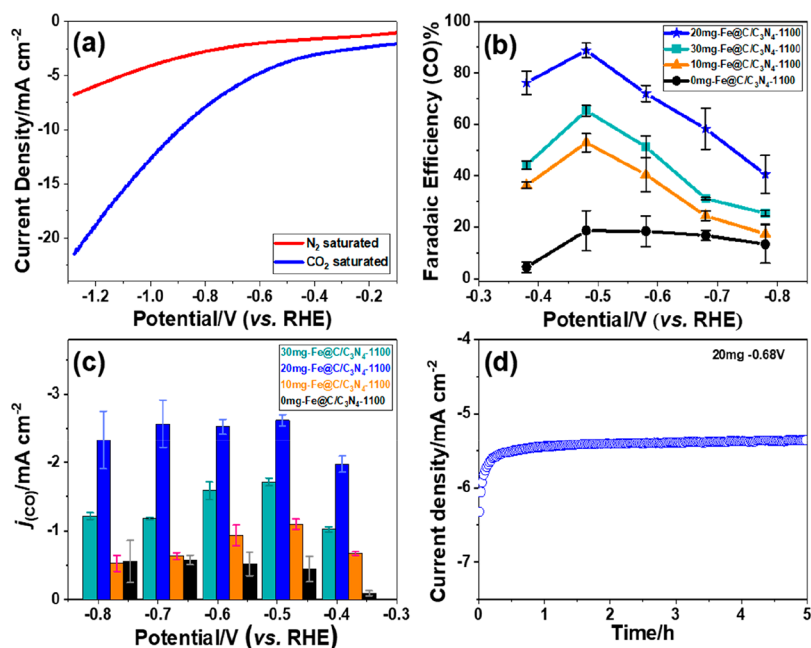
Figure 4. (a) LSV of a 20 mg-Fe@C/C$_3$N$_4$-1100 electrode in N$_2$- and CO$_2$-saturated 0.1 M KHCO$_3$ solutions. (b) Faradaic efficiency (FE) of CO at different potentials for 0 mg-Fe@C/C$_3$N$_4$-1100, 10 mg-Fe@C/C$_3$N$_4$-1100, 20 mg-Fe@C/C$_3$N$_4$-1100, and 30 mg-Fe@C/C$_3$N$_4$-1100. (c) CO current densities at different potentials and (d) stability tests of a 20 mg-Fe@C/C$_3$N$_4$-1100 electrode at −0.68 V vs the RHE for 5 h.
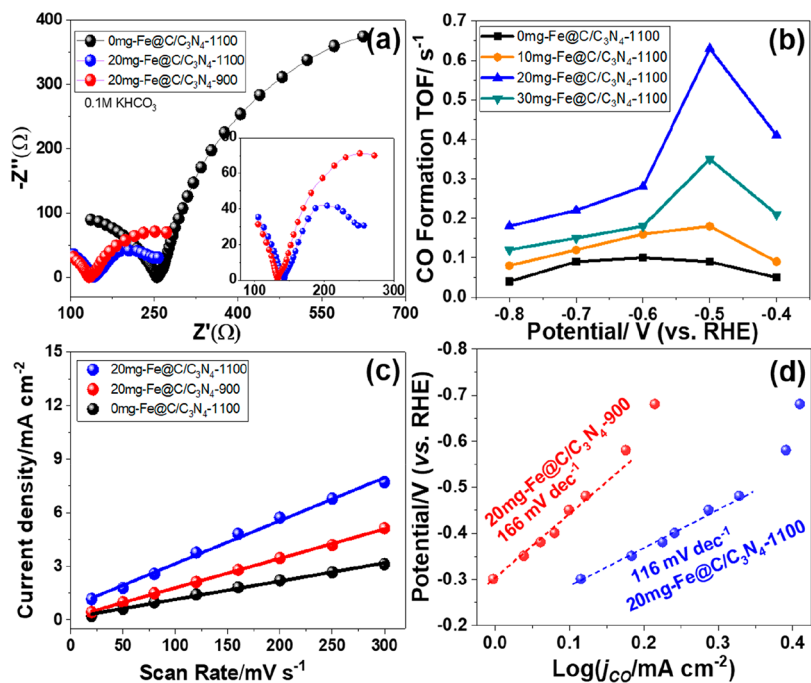
Figure 5. (a) EIS Nyquist plots of 0 mg-Fe@C/C$_3$N$_4$-1100, 20 mg-Fe@C/C$_3$N$_4$-900, and 20 mg-Fe@C/C$_3$N$_4$-1100. (b) The CO formation TOFs of 0 mg-Fe@C/C$_3$N$_4$-1100, 10 mg-Fe@C/C$_3$N$_4$-1100, 20 mg-Fe@C/C$_3$N$_4$-1100, and 30 mg-Fe@C/C$_3$N$_4$-1100 at different potentials. (c) C$_{dl}$ values of 0 mg-Fe@C/C$_3$N$_4$-1100, 20 mg-Fe@C/C$_3$N$_4$-900, and 20 mg-Fe@C/C$_3$N$_4$-1100. (d) Tafel plots for the CO production on 20 mg-Fe@C/C$_3$N$_4$-1100 and 20 mg-Fe@C/C$_3$N$_4$-900, where j_{CO} is the partial current density of CO.

−0.1 to −1.3 V vs the RHE at a scan rate of 0.1 V s^{-1}. As shown in Figure 4a, the as-prepared electrode displayed a potential of −0.6 V$_{RHE}$ at 5 mA cm^{-2} under CO$_2$-saturated conditions in comparison with −1.1 V$_{RHE}$ in an N$_2$-saturated solution. Thus, it can be seen expressly that the prepared electrode was active for CO$_2$ reduction.[35] When a solution was saturated with CO$_2$, there was a shift in the onset potential

toward lower negative potentials along with an increased current density due to the electroreduction of CO$_2$.

More notably, the Faradaic efficiencies toward CO (CO-FE) for the various kinds of Fe@C/C$_3$N$_4$-1100 catalysts as a function of the applied potential are given in Figure 4b. On comparison of the Faradaic efficiencies of CO produced by the four electrodes, it can be seen that the Fe@C/C$_3$N$_4$-1100 electrodes in 0.1 M KHCO$_3$ with an increasing applied

potential revealed that the FE CO increased in a potential window between −0.38 and −0.48 V (vs RHE), reaching a maximum, and then decreased between −0.48 and −0.78 V (vs RHE). Simultaneously, the 20 mg-Fe@C/C$_3$N$_4$-1100 electrode had a higher Faradaic efficiency, attaining a maximum of 88% at −0.48 V. However, CO and H$_2$ are the only gaseous products and no other gaseous species could be detected by online gas chromatography (GC).[36] It is worth noting that a 20 mg-Fe@C/C$_3$N$_4$-1100 electrode had an excellent selectivity for CO (FE CO, 88%) with a low overpotential. Interestingly, Figure 4c provided the partial current densities of CO for 0 mg-Fe@C/C$_3$N$_4$-1100, 10 mg-Fe@C/C$_3$N$_4$-1100, 20 mg-Fe@C/C$_3$N$_4$-1100, and 30 mg-Fe@C/C$_3$N$_4$-1100 catalysts. One can see that the 20 mg-Fe@C/C$_3$N$_4$-1100 catalyst offered a higher CO current density in comparison to the other catalysts, implying a higher CO production capacity.[37]

As the stability of electrodes for the ECR is a vital element to measure the prospective practical applications,[38] the stability of the 20 mg-Fe@C/C$_3$N$_4$-1100 electrode was tested in 0.1 M KHCO$_3$ at −0.68 V *vs*. RHE by using a proton exchange membrane pretreatment to segregate the anode and cathode chambers. Figure 4d showed that a current density of ~5.5 mA cm^{-2} on the 20 mg-Fe@C/C$_3$N$_4$-1100 catalyst was almost completely maintained during 5 h of continuous electrochemical reduction, indicating that this electrode had a stable nature.

The charge transfer resistance at the electrolyte interface can be depicted on the grounds of the arc radius of a Nyquist curve acquired by EIS, where the charge transfer resistance decreases with decreasing arc radius. The Nyquist curves obtained for 20 mg-Fe@C/C$_3$N$_4$ with different sintering temperatures and 0 mg-Fe@C/C$_3$N$_4$-1100 are shown in Figure 5a. It was clearly demonstrated that the 20 mg-Fe@C/C$_3$N$_4$-1100 had the lowest charge transfer impedance (R_{ct}) with the order being 20 mg-Fe@C/C$_3$N$_4$-1100 < 20 mg-Fe@C/C$_3$N$_4$-900 < 0 mg-Fe@C/C$_3$N$_4$-1100. This result was consistent with the experimental observation that the addition of Fe nanoparticles promoted the electron transfer and current density.[39] Prior research indicated that catalysts with lower R_{ct} values had lower charge-transfer resistance between the reactant and the surface of the catalyst, providing a fast pathway for transferring electrons to CO$_2$ in order to generate CO$_2$$^{\bullet}$ intermediates.

The CO formation turnover frequency (TOF) was measured for the presite activity of the catalyst material to generate CO (Figure 5b). Prominently, the TOF of 20 mg-Fe@C/C$_3$N$_4$-1100 was 0.63 s^{-1} versus 0.18 s^{-1} for 10 mg-Fe@C/C$_3$N$_4$-1100 and 0.35 s^{-1} for 20 mg-Fe@C/C$_3$N$_4$-1100 at −0.5 V vs RHE. Nevertheless, the CO formation TOF was only 0.09 s^{-1} for C/C$_3$N$_4$-1100 at −0.5 V vs RHE, implying that the pure C/C$_3$N$_4$-1100 catalyst produced little CO in the CO$_2$ reduction.

The electrochemical active surface areas (ECSAs) of 0 mg-Fe@C/C$_3$N$_4$-1100 and 20 mg-Fe@C/C$_3$N$_4$ at different temperatures were investigated using the electrochemical double layer capacitance (C_{dl}), which were tested with cyclic voltammetry (Figure 4c).[40] The C_{dl} value of 20 mg-Fe@C/C$_3$N$_4$-1100 was 24.1 mF/cm^2, higher than those of C/C$_3$N$_4$-1100 (12.6 mF/cm^2) and 20 mg-Fe@C/C$_3$N$_4$-900 (14.5 mF/cm^2), demonstrating large amounts of exposed active sites for 20 mg-Fe@C/C$_3$N$_4$-1100 during the ECR process.[41]

Furthermore, the Tafel slopes could be procured from LSV curves to explore the kinetics and possible mechanism for ECR on 20 mg-Fe@C/C$_3$N$_4$ catalysts at different temperatures.

Slopes of 116 and 166 mV dec^{-1} were fitted for 20 mg-Fe@C/C$_3$N$_4$-1100 and 20 mg-Fe@C/C$_3$N$_4$-900 (Figure 4d), implying that 20 mg-Fe@C/C$_3$N$_4$-1100 had a faster increment of the CO$_2$ reduction rate with increasing overpotential.[29,42] Simultaneously, this result reveals that the first electron transfer, which gives the surface-adsorbed *COOH intermediate, was the rate-determining step for 20 mg-Fe@C/C$_3$N$_4$-1100 during the ECR.

Results of the studies on the electrocatalytic reduction of CO$_2$ to CO on different electrocatalysts are given in Table 1. It is worth noting that 20 mg-Fe@C/C$_3$N$_4$-1100 showed high selectivity at a low potential, thus proving its enormous potential for electrocatalytic CO$_2$ performance.

Table 1. Comparison with Different Electrocatalysts for CO$_2$ Reduction to CO[a]

catalyst	potential vs RHE (V)	electrolyte	FE (%)	ref
20 mg-Fe@C/g-C$_3$N$_4$-1100	−0.38	0.1 M KHCO$_3$	88	this work
Co$_1$-N$_4$	−0.8	0.1 M KHCO$_3$	82	43
F-CPC	−1	0.5 M KHCO$_3$	88.3	44
Fe−N−C	−0.46	0.5 M KHCO$_3$	85	45
w-CCG/CoPc-A	−0.79	0.1 M KHCO$_3$	91.5	46
NPCM-1000	−0.55	0.5 M KHCO$_3$	92	47
ZIF-A-LD	−1.1	0.1 M KHCO$_3$	90.57	48
Bi$_6$Pd$_{94}$-SAA NDs	−0.4	0.5 M KHCO$_3$	90.5	49
Fe/NG-750	−0.57	0.1 M KHCO$_3$	80	50

[a]Abbreviations: fluorine-doped cagelike porous carbon, F-CPC; "washed" Co(II) phthalocyanine chemically converted graphene, w-CCG/CoPc-A; nitrogen−phosphorus codoped carbon materials, NPCM; coordination of Zn with N atoms in phenanthroline to form a ligand-doped product, ZIF-A-LD; Bi$_6$−Pd$_{94}$ single atom alloy (SAA) nanodendrites (NDs), Bi$_6$Pd$_{94}$-SAA NDs.

■ CONCLUSION

In this work, a useful ferromagnetic catalyst based on 20 mg-Fe@C/C$_3$N$_4$-1100 has been successfully synthesized. The electrocatalytic activity of the 20 mg-Fe@C/C$_3$N$_4$-1100 composite catalyst is visibly improved by the synergistic effect between g-C$_3$N$_4$ as the supporting substrate and iron particles with highly active sites heightening the transfer of charge, leading to a maximum FE of 88% for CO and a low overpotential of −0.38 V vs RHE. This is the best selectivity and activity for CO among many iron-based catalysts reported thus far. The Tafel slopes further display that the 20 mg-Fe@C/C$_3$N$_4$-1100 catalyst stabilizes the *OCOOH intermediate more effectively, thus increasing the potential for conversion of CO$_2$ to CO. The present study offers a novel avenue to design potential precatalysts and gives new insights into the application of the ECR.

■ EXPERIMENTAL SECTION

Materials. Ferric acetylacetonate (C$_{15}$H$_{21}$FeO$_6$), Pluronic F-127, and KHCO$_3$ were purchased from Aladdin Industrial Corporation. Melamine (C$_3$H$_6$N$_6$) and concentrated hydrochloric acid (HCl) were purchased from Sinopharm Chemical Reagent Co. Ltd., China, and used without further purification.

Fabrication of g-C$_3$N$_4$. g-C$_3$N$_4$ were successfully synthesized by directly heating melamine. First, melamine was dried at 80 °C for 12 h in an oven. This dried melamine powder was then put into an alumina crucible with a cover and heated to

550 °C in a muffle furnace for 2 h at a heating rate of 5 °C/min. The resulting g-C_3N_4 was then subjected to grinding to increase the specific surface area.

Fabrication of 10 mg-Fe@C/g-C_3N_4-1100. In a typical synthesis of 10 mg-Fe@C/C_3N_4-1100, 3 g of g-C_3N_4, 6 g of Pluronic F-127 (the mass ratio is 1:2) and 10 mg of Fe(acac)$_3$ were uniformly dissolved in 500 mL of deionized water by an ultrasonic treatment for 2 h. After this solution was vigorously stirring for another 6 h, the resultant products were separated by centrifugation and washed three times with ultrapure water and absolute ethanol. Subsequently, the black powder was carbonized in a tube furnace at 1100 °C for 1 h with a heating rate of 5 °C min^{-1} under a N_2 atmosphere (40 mL/min). This powder was suspended in 2 M HCl solution for 24 h and then washed repeatedly with ethanol and ultrapure water to obtain the final sample.

Fabrication of 0 mg-Fe@C/g-C_3N_4-1100, 20 mg-Fe@C/g-C_3N_4-1100, and 30 mg-Fe@C/g-C_3N_4-1100. Typically, the preparation process was similar to that for 10 mg-Fe@C/g-C_3N_4-1100, except that 10 mg of Fe(acac)$_3$ was replaced by 0, 20, or 30 mg Fe(acac)$_3$ for 0 mg-Fe@C/g-C_3N_4-1100, 20 mg-Fe@C/g-C_3N_4-1100, and 30 mg-Fe@C/g-C_3N_4-1100, respectively.

Fabrication of 20 mg-Fe@C/g-C_3N_4-900. The preparation process was the same as that for 10 mg-Fe@C/g-C_3N_4-1100, except that the sintering temperature of 1100 °C was changed to 900 °C for 20 mg-Fe@C/g-C_3N_4-900.

Materials Characterization. The crystal structures, compositions, morphologies, and valence states of elements of the Fe@C/C_3N_4 composite materials were examined by X-ray powder diffraction (XRD), X-ray photoelectron spectroscopy (XPS), scanning electron microscopy (SEM), transmission electron microscopy (TEM), fast Fourier transform (FFT), and H_2-temperature-programmed reduction (TPR). Their abilites to carry out the ECR were appraised under electrochemical conditions, and the reaction products were quantified by Weather Chromatograph, Model SP-2100 A, equipped with a thermal conductivity detector (TCD) and flame ionization detector (FID). These TCD and FID detectors were used to detect H_2 and CO, respectively.

Electrochemical Tests. Electrochemical measurements were conducted with a traditional three-electrode system by means of a CHI 660E workstation (Shanghai Chenhua Instrumental Co., Ltd., China) using a sealed H-cell. An Ag/AgCl electrode was utilized as the reference electrode, and Pt foil served as the counter electrode. An Fe@C/C_3N_4 working electrode with an effective area of 1×1 cm^2 was used for the ECR. In the cathode compartment, the catholyte utilized in our study was 0.1 M KHCO$_3$. Before experiments, the catholyte was purged with N_2 and CO_2 for 30 min; the pHs of 0.1 M KHCO$_3$ saturated with N_2 and CO_2 were 8.3 and 6.7, respectively. To transform all of the potentials to references to the reversible hydrogen electrode (RHE), the following formula was used

$$E(\text{vs RHE}) = E(\text{vs Ag/AgCl}) + 0.197 + 0.0591 \times \text{pH}$$

■ AUTHOR INFORMATION

Corresponding Authors

Chunyang Zhai − *School of Materials Science and Chemical Engineering, Ningbo University, Ningbo 315211, People's Republic of China;* ⊙ orcid.org/0000-0003-0497-0912; Email: zhaichunyang@nbu.edu.cn

Hengcong Tao − *School of Petrochemical Engineering & Environment, Zhejiang Ocean University, Zhoushan 316022, People's Republic of China; SINOPEC Dalian Research Institute of Petroleum and Petrochemicals, Dalian, Liaoning 116045, People's Republic of China; College of Chemical and Biological Engineering, Zhejiang University, Hangzhou 310058, People's Republic of China;* ⊙ orcid.org/0000-0002-8893-9623; Email: hengcongtao@zjou.edu.cn

Authors

Lina Zhang − *School of Petrochemical Engineering & Environment, Zhejiang Ocean University, Zhoushan 316022, People's Republic of China; School of Materials Science and Chemical Engineering, Ningbo University, Ningbo 315211, People's Republic of China*

Ying Zhang − *SINOPEC Dalian Research Institute of Petroleum and Petrochemicals, Dalian, Liaoning 116045, People's Republic of China*

Baikang Zhu − *School of Petrochemical Engineering & Environment, Zhejiang Ocean University, Zhoushan 316022, People's Republic of China; Zhejiang Provincial Key Laboratory of Petrochemical Environmental Pollution Control, Zhoushan, Zhejiang 316022, People's Republic of China*

Jian Guo − *School of Petrochemical Engineering & Environment, Zhejiang Ocean University, Zhoushan 316022, People's Republic of China*

Dongguang Wang − *School of Petrochemical Engineering & Environment, Zhejiang Ocean University, Zhoushan 316022, People's Republic of China*

Zhongqi Cao − *SINOPEC Dalian Research Institute of Petroleum and Petrochemicals, Dalian, Liaoning 116045, People's Republic of China*

Lihui Chen − *School of Petrochemical Engineering & Environment, Zhejiang Ocean University, Zhoushan 316022, People's Republic of China*

Luhui Wang − *School of Petrochemical Engineering & Environment, Zhejiang Ocean University, Zhoushan 316022, People's Republic of China*

Complete contact information is available at:
https://pubs.acs.org/10.1021/acsomega.1c07298

Author Contributions

Data curation and writing—original draft, L.Z.; investigation, Y.Z.; conceptualization, B.Z.; resources, J.G.; methodology, D.W.; writing—review and editing, Z.C.; validation, L.C.; software, L.W. All authors have read and agreed to the final version of the manuscript.

Notes

The authors declare no competing financial interest.

■ ACKNOWLEDGMENTS

■ REFERENCES

(1) Popovic, S.; Smiljanic, M.; Jovanovic, P.; Vavra, J.; Buonsanti, R.; Hodnik, N. Stability and Degradation Mechanisms of Copper-Based

Catalysts for Electrochemical CO_2 Reduction. *Angew. Chem., Int. Ed.* **2020**, *59*, 14736−14746.

(2) Zhang, S.; Fan, Q.; Xia, R.; Meyer, T. J. CO_2 Reduction: From Homogeneous to Heterogeneous Electrocatalysis. *Acc. Chem. Res.* **2020**, *53*, 255−264.

(3) Li, X. D.; Wang, S. M.; Li, L.; Sun, Y. F.; Xie, Y. Progress and Perspective for In Situ Studies of CO_2 Reduction. *J. Am. Chem. Soc.* **2020**, *142*, 9567−9581.

(4) He, J.; Johnson, N.; Huang, A.; Berlinguette, C. P. Electrocatalytic Alloys for CO_2 Reduction. *ChemSusChem.* **2018**, *11*, 48−57.

(5) Li, M. H.; Wang, H. F.; Luo, W.; Sherrell, P. C.; Chen, J.; Yang, J. P. Heterogeneous Single-Atom Catalysts for Electrochemical CO2 Reduction Reaction. *Adv. Mater.* **2020**, *32*, 2001848.

(6) Wei, B.; Xiong, Y. S.; Zhang, Z. Y.; Hao, J.; Li, L. H.; Shi, W. D. Efficient electrocatalytic reduction of CO_2 to HCOOH by bimetallic In-Cu nanoparticles with controlled growth facet. *Appl. Catal., B* **2021**, *283*, 119646.

(7) Zhang, Y.; Jiao, L.; Yang, W.; Xie, C. F.; Jiang, H. J. Rational Fabrication of Low-Coordinate Single-Atom Ni Electrocatalysts by MOFs for Highly Selective CO_2 Reduction. *Angew. Chem., Int. Ed.* **2021**, *60*, 7607−7611.

(8) Resasco, J.; Bell, A. T. Electrocatalytic CO_2 Reduction to Fuels: Progress and Opportunities. *Trends in Chemistry.* **2020**, *2*, 825−836.

(9) Zhang, B. H.; Jiang, Y. Z.; Gao, M. X.; Ma, T.; Pan, H. Recent progress on hybrid electrocatalysts for efficient electrochemical CO_2 reduction. *Nano Energy.* **2021**, *80*, 105504.

(10) Yang, F.; Ma, X. Y.; Cai, W. B.; Song, P.; Xu, W. L. Nature of Oxygen-Containing Groups on Carbon for High-Efficiency Electrocatalytic CO_2 Reduction Reaction. *J. Am. Chem. Soc.* **2019**, *141*, 20451−20459.

(11) Pan, F. P.; Li, B. Y.; Deng, W.; Du, Z. C.; Gang, Y.; Wang, G. F.; Li, Y. Promoting electrocatalytic CO_2 reduction on nitrogen-doped carbon with sulfur addition. *Appl. Catal., B* **2019**, *252*, 240−249.

(12) Ye, L.; Ying, Y. R.; Sun, D. G.; Zhang, Z. Y.; Fei, L. F.; Wen, Z. H.; Qiao, J. L.; Huang, H. T. Highly Efficient Porous Carbon Electrocatalyst with Controllable N-Species Content for Selective CO_2 Reduction. *Angew. Chem., Int. Ed.* **2020**, *59*, 3244−3251.

(13) Pan, F. P.; Li, B. Y.; Sarnello, E.; Fei, Y. H.; Gang, Y.; Xiang, X. M.; Du, Z. C.; Zhang, P.; Wang, G. F.; Nguyen, H. T.; Li, T.; Hu, H. T.; Zhou, H. C.; LI, Y. Atomically Dispersed Iron-Nitrogen Sites on Hierarchically Mesoporous Carbon Nanotube and Graphene Nanoribbon Networks for CO_2 Reduction. *ACS Nano* **2020**, *14*, 5506−5516.

(14) Pan, Y.; Lin, R.; Chen, Y. J.; Liu, S. J.; Zhu, W.; Cao, X.; Chen, W. X.; Wu, K. L.; Cheong, W. C.; Wang, Y.; Zheng, L. R.; Luo, J.; Lin, Y.; Liu, Y. Q.; Liu, C. G.; Li, J.; Q. L.; Chen, X.; Wang, D. S.; Peng, Q.; Chen, C.; Li, Y. D. Design of Single-Atom Co-N₅ Catalytic Site: A Robust Electrocatalyst for CO_2 Reduction with Nearly 100% CO Selectivity and Remarkable Stability. *J. Am. Chem. Soc.* **2018**, *140*, 4218−4221.

(15) Lu, P. L.; yang, Y. J.; Yao, J. N.; Wang, M.; Dipazir, S.; Yauan, M. G.; Zhang, J. X.; Wang, X.; Xie, Z. J.; Zhang, G. J. Facile synthesis of single-nickel-atomic dispersed N-doped carbon framework for efficient electrochemical CO_2 reduction. *Appl. Catal., B* **2019**, *241*, 113−119.

(16) Sato, S.; Saita, K.; Sekizawa, K.; Maeda, S.; Morikawa, T. Low-Energy Electrocatalytic CO_2 Reduction in Water over MnComplex Catalyst Electrode Aided by a Nanocarbon Support and K⁺ Cations. *ACS Catal..* **2018**, *8*, 4452−4458.

(17) Pan, F. P.; Deng, W.; Justiniano, C.; Li, Y. Identification of champion transition metals centers in metal and nitrogen-codoped carbon catalysts for CO_2 reduction. *Appl. Catal., B* **2018**, *226*, 463−472.

(18) Ao, C. C.; Feng, B. B.; Qian, S. Y.; Wang, L.; Zhao, W.; Zhai, Y. T.; Zhang, L. D. Theoretical study of transition metals supported on g-C_3N_4 as electrochemical catalysts for CO_2 reduction to CH_3OH and CH_4. *J. CO2 Util.* **2020**, *36*, 116−123.

(19) Woyessa, G. W.; Cruz, J. B.; Rameez, M.; Hung, C. H. Nanocomposite catalyst of graphitic carbon nitride and Cu/Fe mixed metal oxide for electrochemical CO_2 reduction to CO. *Appl. Catal., B* **2021**, *291*, 120052.

(20) Cai, J. D.; Huang, Y. J.; Guo, Y. L. $PdTe_x$/C nanocatalysts with high catalytic activity for ethanol electro-oxidation in alkaline medium. *Appl. Catal., B* **2014**, *150−151*, 230−237.

(21) Tao, T. H.; Sun, X. F.; Back, S.; Han, Z. S.; Zhu, Q. G.; Robertson, A. W.; Ma, T.; Fan, Q.; Han, B. X.; Jung, Y. S.; Sun, Z. Y. Doping palladium with tellurium for the highly selective electrocatalytic reduction of aqueous CO_2 to CO. *Chem. Sci.* **2018**, *9*, 483−487.

(22) Jiang, W. J.; Gu, L.; Li, L.; Zhang, Y.; Zhang, X.; Zhang, L. J.; Wang, J. Q.; Song, H. J.; Wei, Z.; Wan, L. J. Understanding the High Activity of Fe-N-C Electrocatalysts in Oxygen Reduction: Fe/Fe₃C Nanoparticles Boost the Activity of Fe-Nₓ. *J. Am. Chem. Soc.* **2016**, *138*, 3570−3578.

(23) Sun, X. P.; Wei, P.; Gu, S. Q.; Zhang, J. X.; Jiang, Z.; Wan, J.; Chen, Z. Y.; Huang, L.; Xu, Y.; Fang, C.; Li, Q.; Han, J. T.; Huang, Y. H. Atomic-Level Fe-N-C Coupled with Fe₃C-Fe Nanocomposites in Carbon Matrixes as High-Efficiency Bifunctional Oxygen Catalysts. *Small.* **2020**, *16*, 1906057.

(24) Han, J. X.; Bao, H. L.; Wang, J. Q.; Zheng, L. R.; Sun, S. R.; Wang, Z. L.; Sun, C. W. 3D N-doped ordered mesoporous carbon supported single-atom Fe-N-C catalysts with superior performance for oxygen reduction reaction and zinc-air battery. *Appl. Catal., B* **2021**, *280*, 119411.

(25) Sharma, L.; Purdy, S. C.; Page, K.; Rangarajan, S.; Pham, H.; Datye, A.; Baltrusaitis, J. Sulfur Tolerant Subnanometer Fe/Alumina Catalysts for Propane Dehydrogenation. *ACS Appl. Nano Mater..* **2021**, *4*, 10055−10067.

(26) Huang, X. J.; Duan, Y. F.; Meng, J. I.; Wu, X.; Zhao, W. M.; Hu, P.; Zhu, C.; Wei, H. Q.; Ma, Y. G. Influence of calcination temperature on SO_2 resistance of Mn-Fe-Sn/TiO_2 catalysts at low-temperature. *Asia-Pac J. Chem. Eng.* **2021**, *16*, No. e2587.

(27) Apostolescu, N.; Geiger, B.; Hizbullah, K.; Jan, M. T.; Kureti, S.; Reichert, D.; Schott, F.; Weisweiler, W. Selective catalytic reduction of nitrogen oxides by ammonia on iron oxide catalysts. *Appl. Catal., B* **2006**, *62*, 104−114.

(28) Zhao, L.; Zhang, Y.; Huang, L. B.; Liu, X. Z.; Zhang, Q. H.; He, C.; Wu, Z. Y.; Zhang, L. J.; Wu, J. P.; Yang, W. I.; Gu, L.; Hu, J. S.; Wan, L. J. Cascade anchoring strategy for general mass production of high-loading single-atomic metal-nitrogen catalysts. *Nat. Commun.* **2019**, *10*, 1278.

(29) Ni, W. P.; Liu, Z. X.; Zhang, Y.; Ma, C.; Deng, H. Q.; Zhang, S. G.; Wang, S. Y. Electroreduction of Carbon Dioxide Driven by the Intrinsic Defects in the Carbon Plane of a Single Fe-N₄ Site. *Adv. Mater.* **2021**, *33*, 2003238.

(30) Tuo, J. Q.; Lin, Y. X.; Zhu, Y. H.; Jiang, H. I.; Li, Y. H.; Cheng, L.; Panga, R.; Shena, J. H.; Song, L.; Li, C. Z. Local structure tuning in Fe-N-C catalysts through support effect for boosting CO_2 electroreduction. *Appl. Catal., B* **2020**, *272*, 118960.

(31) Rehani, D.; Bishnoi, S.; Saxen, M.; Sharmab, S. N. Optimized Fe-doped ZnO nanoparticles for magneto-opto device applications. *Materials Today: Proceedings.* **2020**, *32*, 417−421.

(32) Esmaeili, H.; Mousavi, S. M.; Hashemi, S. A.; Chiang, W. H.; Abnavi, S. A. Activated carbon@MgO@Fe_3O_4 as an efficient adsorbent for As (III) removal. *Carbon Lett.* **2021**, *31*, 851−862.

(33) Katiyar, A.; Dhar, P.; Nandi, T.; Das, S. K. Enhanced heat conduction characteristics of Fe, Ni and Co nanofluids influenced by magnetic field. *Exp. Therm. Fluid Sci.* **2016**, *78*, 345−353.

(34) Yadav, A. N.; Bindra, J. K.; Jakhar, N.; Singh, K. Switching-on superparamagnetism in diluted magnetic Fe(III) doped CdSe quantum dots. *CrystEngComm.* **2020**, *22*, 1738−1745.

(35) Zhang, H. N.; Li, J.; Xi, S. B.; Du, Y. H.; Hai, X.; Wang, J. Y.; Xu, H. M.; Wu, G.; Zhang, J.; Lu, J.; Wang, J. Z. A Graphene-Supported Single-Atom FeN₅ Catalytic Site for Efficient Electrochemical CO_2 Reduction. *Angew. Chem.* **2019**, *131*, 15013−15018.

(36) Pan, F. P.; Li, B. Y.; Sarnello, E.; Fei, Y. H.; Gang, Y.; Xiang, X. M.; Du, Z. C.; Zhang, P.; Wang, G. F.; Nguyen, H. T.; Li, T.; Hu, Y. H.; Zhou, H. C.; Li, Y. Atomically Dispersed Iron-Nitrogen Sites on Hierarchically Mesoporous Carbon Nanotube and Graphene Nano-ribbon Networks for CO_2 Reduction. *ACS Nano* **2020**, *14*, 5506−5516.

(37) Pan, F.; Zhao, H.; Deng, W.; Feng, X.; Li, Y. A novel N,Fe-Decorated carbon nanotube/carbon nanosheet architecture for efficient CO_2 reduction. *Electrochim. Acta* **2018**, *273*, 154−161.

(38) Yang, F.; Jiang, C.; Ma, M.; Shu, F.; Mao, X.; Yu, W.; Wang, J.; Zeng, Z.; Deng, S. Solid-state synthesis of Cu nanoparticles embedded in carbon substrate for efficient electrochemical reduction of carbon dioxide to formic acid. *Chem. Eng. J.* **2020**, *400*, 125879.

(39) Abdinejad, M.; Dao, C. l.; Deng, B. L.; Sweeney, M. E.; Dielmann, F.; Zhang, X. A.; Kraatz, H. B. Enhanced Electrochemical Reduction of CO_2 to CO uponImmobilization onto Carbon Nanotubes Using an Iron-Porphyrin Dimer. *ChemistrySelect.* **2020**, *5*, 979−984.

(40) Pan, F.; Li, B.; Sarnello, E.; Fei, Y.; Feng, X.; Gang, Y.; Xiang, X.; Fang, L.; Li, T.; Hu, Y. H.; Wang, G.; Li, Y. Pore-Edge Tailoring of Single-Atom Iron-Nitrogen Sites on Graphene for Enhanced CO_2 Reduction. *ACS Catal.* **2020**, *10*, 10803−10811.

(41) Zhang, C. H.; Yang, S. Z.; Wu, J. J.; Liu, M. J.; Yazdi, S.; Ren, M.; Sha, J. w.; Zhong, J.; Nie, K. q.; Jalilov, A. S.; et al. Electrochemical CO_2 Reduction with Atomic Iron-Dispersed on Nitrogen-Doped Graphene. *Adv. Energy Mater.* **2018**, *8*, 1703487.

(42) Ju, W.; Bagger, A.; Wang, X.; Tsai, Y.; Luo, F.; Moller, T.; Wang, H.; Rossmeisl, J.; Varela, A. S.; Strasser, P. Unraveling Mechanistic Reaction Pathways of the Electrochemical CO_2 Reduction on Fe-N-C Single-Site Catalysts. *ACS Energy Lett.* **2019**, *4*, 1663−1671.

(43) Geng, Z. G.; Cao, Y. J.; Chen, W. X.; Kong, X. D.; Liu, Y.; Yao, T.; Lin, Y. Regulating the coordination environment of Co single atoms for achieving efficient electrocatalytic activity in CO_2 reduction. *Appl. Catal., B* **2019**, *240*, 234−240.

(44) Ni, W.; Xue, Y. F.; Zang, X. G.; Li, C. X.; Wang, H. Z.; Yang, Z. Y.; Yan, Y. M. Fluorine Doped Cagelike Carbon Electrocatalyst: An Insight into the Structure Enhanced CO Selectivity for CO_2 Reduction at High Overpotential. *ACS Nano* **2020**, *14*, 2014−2020.

(45) Hu, X.-M.; Hval, H. H.; Bjerglund, E. T.; Dalgaard, K. J.; Madsen, M. R.; Pohl, M.-M.; Welter, E.; Lamagni, P.; Buhl, K. B.; Bremholm, M.; Beller, M.; Pedersen, S. U.; Skrydstrup, T.; Daasbjerg, K. Selective CO_2 Reduction to CO in Water using Earth-Abundant Metal and Nitrogen-Doped Carbon Electrocatalysts. *ACS Catal..* **2018**, *8*, 6255−6264.

(46) Choi, J.; Wagner, P.; Gambhir, S.; Jalili, R.; MacFarlane, D. R.; Wallace, G. G.; Officer, D. L. Steric Modification of a Cobalt Phthalocyanine/Graphene Catalyst To Give Enhanced and Stable Electrochemical CO_2 Reduction to CO. *ACS Energy Lett.* **2019**, *4*, 666−672.

(47) Chen, S.; Liu, T. F.; Olanrele, S. O.; Lian, Z.; Si, C.; Chen, Z. M.; Li, B. Boosting electrocatalytic activity for CO_2 reduction on nitrogen-doped carbon catalysts by co-doping with phosphorus. *J. Energy Chem.* **2021**, *54*, 143−150.

(48) Dou, S.; Song, J. J.; Xi, S. B.; Du, Y. H.; Wang, J.; Huang, Z. F.; Xu, Z. J.; Wang, X. Boosting Electrochemical CO_2 Reduction on Metal-Organic Frameworks via Ligand Doping. *Angew. Chem..* **2019**, *131*, 4081−4085.

(49) Xie, H.; Wan, Y. Y.; Wang, X. M.; Liang, J. S.; Lu, G.; Wang, T. Y.; Chai, J. L.; Adli, N. M.; Priest, C.; Huang, Y. H.; Wu, G.; Li, Q. Boosting Pd-catalysis for electrochemical CO_2 reduction to CO on Bi-Pd single atom alloy nanodendrites. *Appl. Catal., B* **2021**, *289*, 119783.

(50) Zhang, C. H.; Yang, S. Z.; Wu, J. J.; Liu, M. G.; Yazdi, S.; Ren, M. Q.; DSha, J. W.; Zhong, J.; Nie, K.; Jalilov, A. S.; Li, Z. Y.; Li, H. M.; Yakobson, B. I.; Wu, Q.; Ringe, E.; Xu, H.; Ajayan, P. M.; Tour, J. M. Electrochemical CO_2 Reduction with Atomic Iron-Dispersed on Nitrogen-Doped Graphene. *Adv. Energy Mater.* **2018**, *8*, 1703487.